

## LyC Leakers in the *AstroSat* UV Deep Field: Extreme UV emitters at the Cosmic Noon

SURAJ DHIWAR,<sup>1,2</sup> KANAK SAHA,<sup>1</sup> SOUMIL MAULICK,<sup>1</sup> BRENT M. SMITH,<sup>3</sup> CHAYAN MONDAL,<sup>1</sup> HARRY I. TEPLITZ,<sup>4</sup>  
MARC RAFELSKI,<sup>5,6</sup> AND ROGIER A. WINDHORST<sup>3</sup>

<sup>1</sup>*Inter University Center for Astronomy and Astrophysics, Ganeshkhind, Pune 411007, India*

<sup>2</sup>*Department of Physics, Savitribai Phule Pune University, Pune 411007, India*

<sup>3</sup>*School of Earth and Space Exploration, Arizona State University, Tempe, AZ 85287-1404, USA*

<sup>4</sup>*IPAC, Mail Code 314-6, Caltech, 1200 E. California Blvd., Pasadena, CA 91125, USA*

<sup>5</sup>*Space Telescope Science Institute, 3700 San Martin Drive, Baltimore, MD 21218, USA*

<sup>6</sup>*Department of Physics and Astronomy, Johns Hopkins University, Baltimore, MD 21218, USA*

### ABSTRACT

We report the direct detection of Lyman Continuum (LyC) emission from 9 galaxies and 1 Active Galactic Nuclei (AGN) at  $z \sim 1.1$ - $1.6$  in the GOODS-North field using deep observations from the Ultraviolet Imaging Telescope (UVIT) onboard *AstroSat*. The absolute escape fraction of the sources estimated from the far-ultraviolet (FUV) and H $\alpha$  line luminosities using Monte Carlo (MC) analysis of two Inter-Galactic Medium (IGM) models span a range  $\sim 10$  -  $55$  %. The restframe UV wavelength of the sources falls in the extreme-ultraviolet (EUV) regime  $\sim 550$ - $700$  Å, the shortest LyC wavelength range probed so far. This redshift range remains devoid of direct detections of LyC emission due to the instrumental limitations of previously available facilities. With UVIT having a very low detector noise, each of these sources are detected with an individual signal-to-noise ratio (SNR)  $> 3$  while for the stack of six sources, we achieve an SNR  $\sim 7.4$ . The LyC emission is seen to be offset from the optical centroids and extended beyond the UVIT PSF of  $1.''6$  in most of the sources. This sample fills an important niche between GALEX and Cosmic Origins Spectrograph (COS) at low- $z$ , and HST WFC3 at high- $z$  and is crucial in understanding the evolution of LyC leakers.

*Keywords:* galaxies: emission line — galaxies: high-redshift — reionization — ultraviolet astronomy

### 1. INTRODUCTION

After the Big Bang, the Universe expanded and cooled until the electrons and protons could combine to form atoms (at  $z \sim 1090$ ) and remained in the neutral form until the Cosmic Dawn ( $z \sim 20$ - $15$ ) when the first galaxies started forming. During the period from  $z \sim 12$  to  $z \sim 6$ , when the LyC radiation from the galaxies started ionizing the surrounding Inter-Galactic Medium (IGM), the Universe underwent a transformation from a completely neutral state to an almost completely ionised state; see Robertson et al. (2010) for a review. Detecting the ionizing radiation from this early epoch of galaxies is extremely important to understand the nature and formation of these galaxies and the process of reionization.

However, direct detection of LyC photons from the era of reionization is challenging because of the increasing IGM opacity (Madau 1995; Inoue et al. 2014) and

plausible faintness of the ionizing sources. Nevertheless, there have been detection of LyC emission from local analogues of the high redshift galaxies at  $z < 0.4$  using the Cosmic Origins Spectrograph on the Hubble Space Telescope (Leitet et al. 2013; Borthakur et al. 2014; Izotov et al. 2016; Leitherer et al. 2016; Izotov et al. 2018; Flury et al. 2022), as well at higher redshift  $z > 3$  using HST and ground-based imaging (Shapley et al. 2016; Vanzella et al. 2016; Bian et al. 2017; Steidel et al. 2018; Vanzella et al. 2018; Fletcher et al. 2019; Prichard et al. 2022; Liu et al. 2023).

There was no direct detection of LyC emission in the intermediate redshift range  $0.5 \lesssim z \lesssim 3$  until the UVIT onboard the Indian multiwavelength satellite *AstroSat* detected EUV radiation from a clumpy galaxy (AUDFs01) at  $z \simeq 1.42$  (Saha et al. 2020). Previously, extensive stacking analyses have been carried out using HST/WFC3 deep field data and provided upper limits on the LyC escape fraction in this redshift range, however, with no significant detection of LyC emission (Siana et al. 2007; Iwata et al. 2009; Smith et al. 2018, 2020; Alavi et al. 2020). A larger sample of EUV emitters like AUDFs01 is required to investigate if such

galaxies are representative of the high-redshift galaxies that contributed to the reionization of the Universe.

In this letter, we report the direct detection of LyC emission in the EUV domain (550 – 700 Å) from nine star-forming (SF) galaxies and one hosting an Active Galactic Nucleus (AGN) at the cosmic noon ( $z \sim 1.1-1.6$ ) in the GOODS-North field using deep UV imaging from UVIT (Mondal et al. 2023).

Throughout this work, all distance dependent quantities use  $H_0 = 70 \text{ km s}^{-1} \text{ Mpc}^{-1}$ ,  $\Omega_m = 0.3$ , and  $\Omega_\Lambda = 0.7$  following  $\Lambda$ CDM cosmology.

## 2. DATA

### 2.1. UVIT Imaging data

The far-ultraviolet (FUV) and near-ultraviolet (NUV) imaging data come from AstroSat observations of the GOODS-North field (GT08-77; principal investigator, Kanak Saha). These observations were carried out by UVIT (with a field of view (FOV) of 28' diameter) onboard AstroSat, which performed simultaneous observation in the F154W ( $\lambda_{mean}=1541 \text{ \AA}$ ,  $\Delta\lambda=380 \text{ \AA}$ ) and N242W ( $\lambda_{mean}=2418 \text{ \AA}$ ,  $\Delta\lambda=785 \text{ \AA}$ ) bands during 10 - 12 March, 2018. The observations were carried out for 40 kilosec, which corresponds to  $\sim 32$  orbits. During each orbit, FUV and NUV observations in photon counting mode were taken every 33 ms, resulting in about 45,000–50,000 frames (in each band) accumulation in a good orbit. The final science-ready images of the AstroSat Ultra-violet Deep Field North (AUDFn) had a total exposure time of  $t_{exp} = 34022 \text{ s}$  in the FUV and 19228 s in the NUV with  $5\sigma$  limiting magnitude 26.79 and 26.73, respectively. We ask the reader to refer to Mondal et al. (2023) for more details on the data reduction.

### 2.2. 3DHST grism and Imaging data

We make use of the archival grism spectral data from the 3D-HST survey (PI : Weiner, Brammer et al. 2012; Momcheva et al. 2016). 3D-HST provides rest-frame optical spectra for a sample of  $\sim 7000$  galaxies at  $1 < z < 3.5$ . It covers three-quarters ( $625 \text{ arcmin}^2$ ) of the CANDELS Treasury survey area with two orbits of primary WFC3/G141 grism coverage and two to four orbits with the ACS/G800L grism in parallel. The WFC3/G141 spectra provide continuous wavelength coverage from 1.1 to  $1.65 \mu\text{m}$  at a spatial resolution of  $\sim 0.13''$ . We also make use of the publicly available deep imaging data in optical HST ACS (Giavalisco et al. 2004), IR from WFC3 (Skelton et al. 2014; Koekemoer et al. 2011; Grogin et al. 2011) and U-band from the Mosaic camera on the Kitt Peak 4-m telescope (Capak et al. 2004) of the GOODS-North field.

### 2.3. Sample selection

The spectral data from 3DHST G141 grism is used to identify sources at redshift  $1.0 < z < 2.0$ . We use the  $\text{H}\alpha$

and [OIII]5007 (hereafter [OIII]) lines having line fluxes with  $\text{SNR} > 3$  to identify emission line sources. In the G141 grism with a wavelength coverage of 1.10 - 1.65  $\mu\text{m}$ , the  $\text{H}\alpha$  and [OIII] lines are simultaneously observed only between the redshift range  $z \sim 1.1-1.6$ , restricting the redshift range of the sources to  $1.1 < z < 1.6$  (the redshifts are confirmed with the  $\text{H}\alpha$  and OIII[5007] lines in the grism spectra, whose analysis is discussed in detail in Section 5. Of the 178 sources found from 3DHST grism data, 56 sources are identified in UVIT F154W band images. We perform photometry and the appropriate background estimation of these 56 potential LyC leaker candidates (described in Section 3). To avoid contamination, we consider only the sources having no neighboring companions within  $1.2''$  radius in the Skelton et al. (2014) catalog. In addition to checking the catalog, we also visually inspect the HST F435W and F160W bands for any contaminations within  $1.2''$  radius. With these criteria and requiring the FUV  $\text{SNR} > 3$ , we are left with 11 sources. One source in these 11 is observed to have an  $\text{H}\alpha$  line at the edge of the spectral coverage of G141. To avoid the uncertainty in redshift and line flux measurement, we exclude this source from our sample. We consider the remaining sample of 10 sources as our final sample of LyC leakers. The locations of the 10 detected LyC leakers in GOODS-North field are shown in Figure A.1. We further segregate the sample of 10 LyC leakers into the ones having LyC emission within UVIT PSF FWHM  $\sim 1''.6$  (7 sources) and sources having extended emission beyond  $1''.6$  (3 sources). The UVIT F154W, N242W, HST F160W and HST F435W (convolved with the UVIT FUV PSF) images of the 7 sources are shown in Figure 1, while the extended sources are shown in Figure 5.

We note that one of the LyC leakers in the sample (goodsn-36-G141-25099) has a very narrow  $\text{H}\alpha$  line and rather looks like a noise peak, which could affect the LyC escape fraction and SFR calculations, however the redshift estimated (1.52) from the grism spectra ([OIII] and  $\text{H}\alpha$  lines) is very close to the photometric redshift (1.56) provided in the Skelton et al. (2014) catalog. This implies that the line identification is correct and redshift of the source is likely to be  $z \sim 1.52$ .

## 3. PHOTOMETRIC ANALYSIS

For the 56 potential LyC candidates chosen using the  $\text{H}\alpha$  and [OIII] line emission criteria, we estimate the SNR at their respective positions in the F154W filter of the UVIT. The first step involves estimating the local background around each source. For this, we run Source Extractor (Bertin & Arnouts 1996) on the  $30'' \times 30''$  ( $75 \times 75$  pixels) cutouts around the source. We then place boxes of size  $7 \times 7$  pixels at 10 random locations where there are no sources detected. The  $7 \times 7$  box size is optimally chosen as it is  $\sim$ twice the PSF in UVIT F154W band. The parameters used for generating the SExtractor segmentation maps are listed in

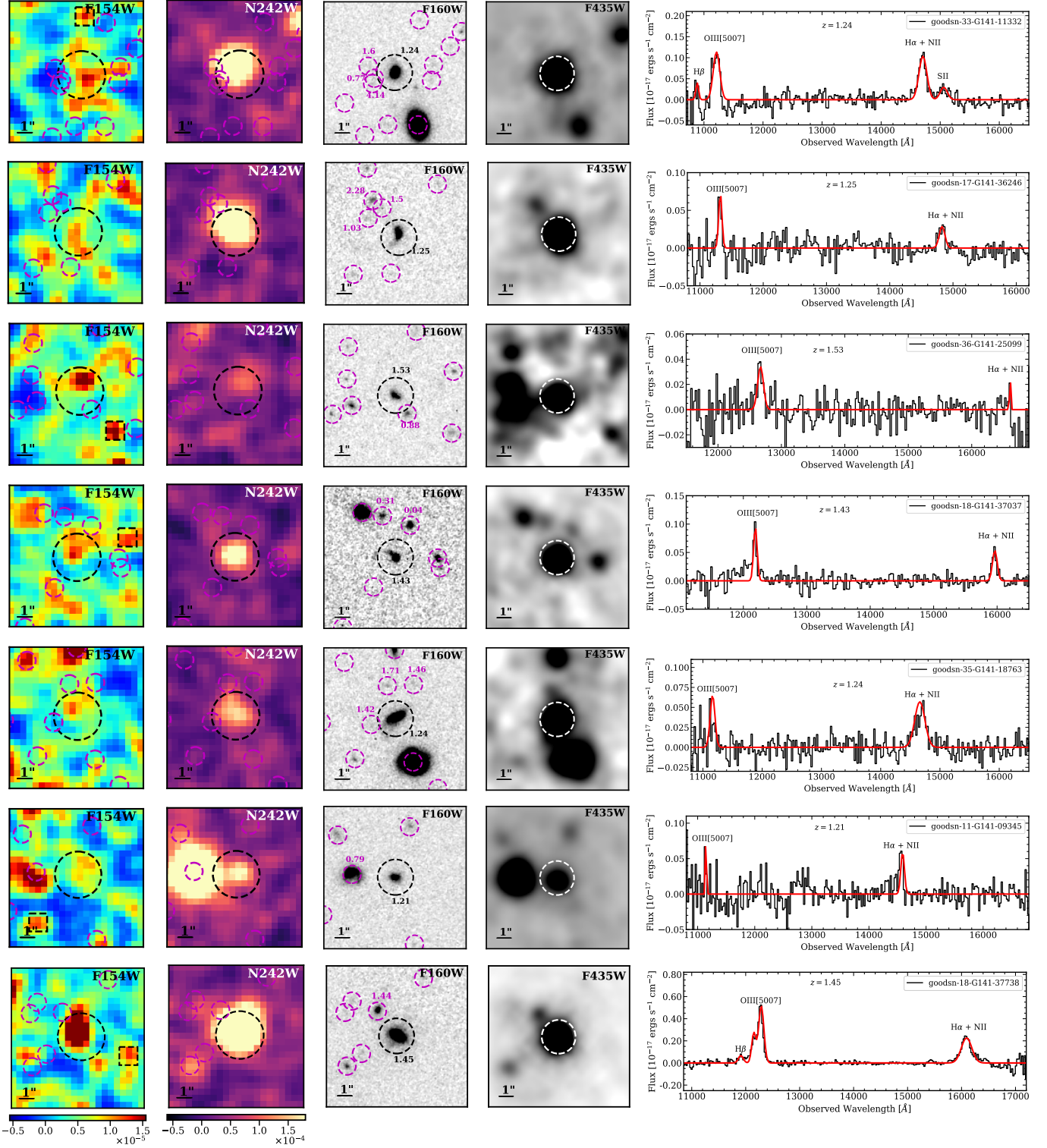


**Figure 1.** The first two panels from the left show the UVIT F154W and N242W band images of the LyC leakers. In the images, North is up and East is towards the left. The black dashed circles on the UVIT images represent apertures of size  $1''.6$  with the same centres as in the HST/F160W images on the right (third) panel. In the HST/F160W band images, these apertures are of size  $1''$  and are centred about the LyC emitters. The magenta circles indicate neighbouring objects. The numbers outside the apertures indicate the redshift of the respective objects close to the LyC leakers. The fourth panel shows the HST/F435W images convolved with the F154W PSF for a size comparison. Spurious sources (see Section 4) are highlighted by dashed black squares in the F154W band. We quote the magnitude (SNR) of such sources from top to bottom: On the first row in the north: 27.07 (1.88), third row in the south-west: 26.50 (2.77); fourth row in the west 26.54 (2.69); sixth row in the south-east: 27.05 (1.93) and seventh row in the south-west: 26.76 (2.38). On the extreme right are the 3D-HST spectra of the LyC leakers. The black solid curves are the original spectra after contamination and continuum subtraction. The red curves indicate the fitted models.

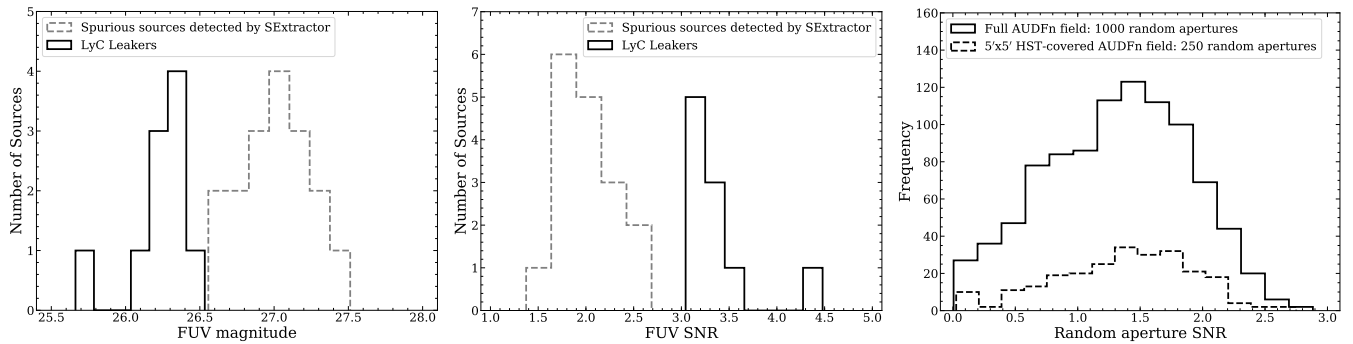


**Figure 2.** *Left panel:* The F154W magnitude of sources detected within  $10'' \times 10''$  field around the 10 LyC leakers by SExtractor. The spurious sources are the ones detected by SExtractor in F154W band around the LyC leakers but not having any counterpart either in HST F435W or F160W band. *Middle panel:* The F154W SNR histogram of the same LyC leakers and the spurious sources as in the left panel. *Right panel:* The SNR distribution of 1000 and 250 circular apertures placed randomly on the entire AUDFn field of  $28'$  diameter (solid line) and  $5' \times 5'$  HST-covered patch (dashed line) respectively, after segmenting the detected sources. Both the histograms show apertures only with positive flux values. All magnitudes and SNRs are calculated based on aperture of radius =  $1.6''$  unless mentioned otherwise.

Table A.1. The mean of these 10 background values is taken as the local background value of the source (The number of random boxes is chosen to be low to avoid overlap, however, a higher number of sampling boxes does not change the background estimate significantly). Then the flux within  $1.6''$  circular aperture placed at the source location is extracted. Using the measured flux, the SNR is then estimated using the relation given in Saha et al. (2020). For one of the sources (goodsn-11-G141\_09345) the SNR estimated within the  $1.6''$  aperture is 2.64, whereas it is 3.10 within an aperture of  $1.2''$ . This could be because of a larger number of noise pixels in the  $1.6''$  aperture. For this particular source we quote the SNR within  $1.2''$  aperture in Table 1. The detection significance and probability of false detections are discussed in Section 4.

Further, AB magnitudes are obtained using the magnitude zero points 17.77 and 19.81 for the F154W and N242W, respectively. The magnitudes are then corrected for foreground dust extinction following Schlafly & Finkbeiner (2011) and internal extinction using the UV beta slope  $f_\lambda \propto \lambda^\beta$  (Reddy et al. 2018), derived from photometry using the Kitt Peak 4-m telescope U band ( $\lambda_{mean} = 3828 \text{ \AA}$ ) and HST F606W ( $\lambda_{mean} = 5921 \text{ \AA}$ ) falling in the rest-wavelength  $\lambda \in [1,268 - 2,580] \text{ \AA}$  using the equation given by (Nordon et al. 2013). The magnitudes and SNR in the F154W band for our final sample of ten LyC leakers are provided in Table 1.

#### 4. DETECTION SIGNIFICANCE OF LYC LEAKERS

In order to check the detection significance of the LyC leakers in the F154W band, we carry out an exercise using SExtractor. We produce  $10'' \times 10''$  cutouts around the 10 detected LyC leakers from the UVIT/F154W deep image. Considering the SExtractor input parameters listed in Table A.1, we identify sources in each

cutout and estimate their magnitude within an aperture of radius  $1''.6$ . In Figure 2 (left panel), we show the magnitude histogram of the LyC leakers, and the SExtractor detected sources that do not have an HST counterpart (termed spurious sources) from all the cutouts. There is a clear segregation in the magnitudes of the spurious sources and the LyC leakers. Further, on the fainter side, we detect sources down to the  $3\sigma$  detection limit ( $27.35 \text{ mag}$ ) in F154W filter as reported by Mondal et al. (2023). The faintest LyC leaker in our sample is around  $\sim 0.8 \text{ mag}$  brighter than the  $3\sigma$  detection limit. It is to be noted here, the  $3\sigma$  detection limit (within an aperture of radius  $1''$ ) is estimated using the average rms noise of the background sky sampled from the entire AUDFn field (see Mondal et al. 2023). Whereas the SNR in this study is estimated using the source signal, local sky background, and exposure time. Following this, the  $3\sigma$  limit is generally fainter than the magnitude of the source having  $\text{SNR} = 3$ . In our case, the  $3\sigma$  detection limit in F154W is  $27.3 \text{ mag}$ , which is fainter than the magnitude of a source having F154W  $\text{SNR} = 3$ .

This signifies that the leaker candidates are unlikely to be spurious noise sources. In the middle panel of Figure 2, we show the SNR distribution of the same sources. The SNR histogram further highlights that the identified LyC leakers have a higher SNR value (i.e., 9 out of 10 with  $\text{SNR} > 3.0$  in  $1.6''$  aperture) compared to a large percentage of spurious sources detected around them.

We carry out an additional independent exercise to test the possibility of false detections in F154W band image. For this, we identify sources in the entire AUDFnorth image (diameter  $\sim 28'$ ) using SExtractor with the parameters listed in Table A.1. Then, 1000 apertures of  $1''.6$  radii are placed randomly such that they do not enclose any segmented pixels identified in the previous step. The mean local background around our 10 leakers

**Table 1.** UV Photometric properties of LyC leakers- Column(1) 3D-HST ID, Column(2): redshift mentioned in the Momcheva et al. (2016) catalog, (the redshift is confirmed by visually inspecting the H $\alpha$  and [OIII] emission lines in the G141 grism spectra), column(3): FUV magnitude corrected for foreground and internal extinction, column(4): SNR of the LyC signal in F154W band within 1.''6 aperture, Column(5) & (6): Mean IGM transmission ( $e^{-\tau}$ ) using (Inoue et al. 2014) and (Bassett et al. 2021), respectively, Column(7): Rest-frame UV wavelength in  $\text{\AA}$  probed by the F154W band, Column(8): LyC (F154W) to UV Continuum (F435W) ratio corresponding to rest frame  $\sim 600\text{-}700 \text{\AA}$  in LyC and  $\sim 1500\text{-}2300 \text{\AA}$  in UVC (Ultraviolet Continuum), Column(9) & (10): Mean LyC escape fractions for the Inoue et al. (2014) and (Bassett et al. 2021) IGM models respectively. The first 7 sources above the horizontal line are the ones where the LyC emission is within a 1.''6 radius aperture, while the objects below the line have signs of extended emission.

3D-HST ID	$z$	$m_{FUV}$ mag	$SNR_{FUV}$	Mean T Inoue	Mean T Bassett	Rest UV $\lambda$ ( $\text{\AA}$ )	$\frac{LyC}{UVC}$	$f_{esc}$ Inoue	$f_{esc}$ Bassett
(1)	(2)	(3)	(4)	(5)	(6)	(7)	(8)	(9)	(10)
goodsn-33-G141_11332	1.24	26.20 $\pm$ 0.35	3.07	0.63	0.39	691	0.62	0.15 $\pm$ 0.04	0.22 $\pm$ 0.02
goodsn-17-G141_36246	1.26	26.22 $\pm$ 0.35	3.12	0.63	0.38	686	0.85	0.56 $\pm$ 0.10	0.67 $\pm$ 0.06
goodsn-36-G141_25099 <sup>a</sup>	1.52	26.21 $\pm$ 0.35	3.09	0.51	0.27	613	4.44	0.79 $\pm$ 0.13	0.88 $\pm$ 0.08
goodsn-18-G141_37037	1.43	26.10 $\pm$ 0.33	3.29	0.54	0.29	636	1.31	0.44 $\pm$ 0.08	0.60 $\pm$ 0.04
goodsn-35-G141_18763	1.24	26.23 $\pm$ 0.35	3.04	0.63	0.39	690	1.62	0.19 $\pm$ 0.05	0.28 $\pm$ 0.03
goodsn-11-G141_09345	1.21	26.43 $\pm$ 0.41	3.10 <sup>b</sup>	0.64	0.40	699	1.41	0.35 $\pm$ 0.09	0.46 $\pm$ 0.06
goodsn-18-G141_37738 <sup>c</sup>	1.45	25.55 $\pm$ 0.24	4.48	0.54	0.27	631	0.69	0.11 $\pm$ 0.02	0.19 $\pm$ 0.01
goodsn-17-G141_35906	1.30	26.11 $\pm$ 0.33	3.27	0.59	0.36	672	2.70	0.36 $\pm$ 0.08	0.48 $\pm$ 0.04
goodsn-46-G141_14637	1.49	26.12 $\pm$ 0.33	3.27	0.51	0.27	622	1.01	0.24 $\pm$ 0.06	0.37 $\pm$ 0.04
goodsn-24-G141_18817	1.49	26.01 $\pm$ 0.31	3.46	0.51	0.27	623	1.19	0.29 $\pm$ 0.06	0.44 $\pm$ 0.04

<sup>a</sup> H $\alpha$  line very narrow,  $f_{esc}$  estimates highly uncertain

<sup>b</sup> SNR measured within 1.''2 aperture radius

<sup>c</sup> AGN

is considered as the background value to construct the SNR distribution of the flux measured within these 1000 random apertures (only positive flux values, Figure 2 right panel). We find no apertures out of 1000 containing flux with  $SNR > 3$ , which indicates that the random fluctuating background pixels are unlikely to mimic an  $SNR > 3$  source flux; see also Borgohain et al. (2022) for a similar outcome from GOODS South F154W deep image. For quantifying the number of FUV spurious sources with respect to the HST detection, we produced a  $5' \times 5'$  cutout of the GOODS-N field in UVIT F154W, N242W, HST F435W, and F160W bands. We created a rescaled UVIT PSF convolved HST detection image combining F435W and F160W bands and used it to produce a segmentation map. We placed 250 random apertures in source free regions guided by this segmentation map. We found less than 4% of the 250 apertures having F154W  $SNR > 3$ . These can either be real FUV sources that are faint in the redder bands or noise peaks in the FUV background. The random aperture exercise using segmentation from UVIT detection is further repeated for this  $5' \times 5'$  cutout with 250 circles and we found a similar result as seen for the entire field (Figure 2 right panel). Further, in  $30'' \times 30''$  area around the LyC leakers, we found  $SNR > 3$  F154W sources and identify their counterpart in HST F435W filter image.

In most cases, we found one-to-one correspondence except goodsn-11-G141\_09345 and goodsn-17-G141\_35906 where F154W (F435W) source numbers are 4(3) and 9(8) respectively.

### 5. SPECTROSCOPIC ANALYSIS

We use the WFC3 G141 grism data for the spectral analysis. We first extract the 1D contamination subtracted spectral data for the 10 shortlisted LyC leaking candidates. For continuum subtraction, we fit the 1D contamination subtracted spectra with a polynomial function using the *specutils* package in PYTHON. All 10 shortlisted LyC leaking candidates show H $\alpha$  and [OIII] lines in emission. The [OIII] is a doublet and is fitted accordingly. The emission line fluxes were estimated by fitting gaussian models to the continuum subtracted observed emission line profiles using the *astropy modelling* package in PYTHON. The uncertainties on the line fluxes were estimated using the error spectrum provided for each object with the 1D G141 grism spectra. Given the error at each wavelength, the error on the line flux was estimated by carrying out standard error propagation of the addition of uncertainties under the line. The region of the spectrum chosen to fall under the line is taken as the same spectral window as that used to fit the Gaussian in the line modeling. In the G141 grism

spectra the  $H\alpha$  line is blended with [NII]. We extract  $H\alpha$  line flux from the blended [NII] line using a method based on equivalent width following (Sobral et al. 2012). Further the [OIII] doublet is also blended and wherever possible we fit a double gaussian to extract the [OIII] line flux (although the estimated [OIII] line fluxes are not used in any of the results in this paper). The obtained line fluxes are further corrected for internal extinction. As most of the galaxies lack  $H\beta$  emission, the UV  $\beta$  slope technique Reddy et al. (2018) is used to correct for the internal extinction. Five of the LyC leakers in the sample show  $H\beta$  line emission. For these galaxies we estimated the  $E(B-V)$  values using the Balmer decrement method by assuming the theoretical ratio as 2.86 assuming Case-B recombination Osterbrock & Bochkarev (1989) with an electron temperature of  $\sim 10^4$  K and electron density of  $100 \text{ cm}^{-3}$ . Only two of the galaxies (goodsn-33-G141\_11332 and goodsn-46-G141\_14637) show positive  $E(B-V)$  values. Assuming a stellar to nebular extinction conversion factor = 0.44, the  $E(B-V)$  for goodsn-33-G141\_11332 using Balmer decrement (0.35) is in close agreement with the estimate from UV  $\beta$  slope method (0.31), while for goodsn-46-G141\_14637 the Balmer decrement gives a lower value. However, it is to be noted that there can be scatter in the relation between stellar and nebular extinction with objects being considerably offset from line with slope  $f = 0.44$  (Koyama et al. 2019; Reddy et al. 2020). Since the number of sources is not sufficient for a statistical comparison and Balmer decrement is not applicable for most of the sources in the sample we use the  $E(B-V)$  estimates from UV  $\beta$  slope. The estimated line fluxes and derived quantities like  $H\alpha$  SFR and sSFR are provided in Table A.2 in Appendix A, while the 1D spectra are shown in extreme right panels of Figure 1 & 5. Further, the  $H\alpha$  line is used to confirm the redshift of the sources.

## 6. ESCAPE FRACTION AND IGM ATTENUATION

To derive the absolute LyC escape fraction, we first estimate the number of hydrogen ionizing photons produced that do not escape the galaxy and are in dynamic equilibrium with the ISM using the dust-corrected luminosity of the  $H\alpha$  recombination line. Assuming a temperature  $T = 10^4$  K and electron density  $n_e = 100 \text{ cm}^{-3}$ , we can estimate the number of LyC photons emitted per unit time that do not escape the galaxy (Osterbrock & Ferland 2006; Saha et al. 2020) as,

$$N_{LyC}^{non-esc} = 7.28 \times 10^{11} L(H\alpha), \quad (1)$$

where  $L(H\alpha)$  is the dust-corrected  $H\alpha$  line luminosity. We estimate the rate at which LyC photons escape the galaxy,  $N_{LyC}^{esc}$  from the FUV flux measured in the F154W filter following Saha et al. (2020). Note that this gives us a lower limit on the number of escaping LyC photons from the galaxy since the FUV band probes only a part of the rest-frame LyC range for our sample.

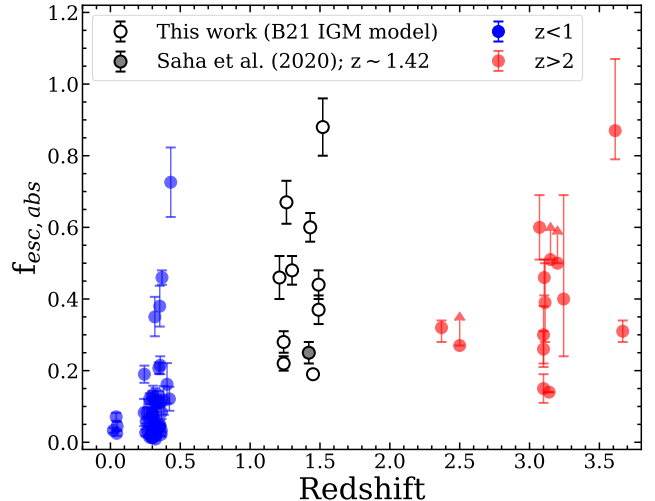


**Figure 3.** The LyC absolute  $f_{esc}$  estimated using Bassett et al. (2021) IGM model in black open circles for the 10 leakers in our sample compared to individual LyC leakers at lower ( $z < 1$ , blue filled circles) and higher redshifts ( $z > 2$ , red filled circles). The low- $z$  leakers are taken from Leitert et al. (2013); Borthakur et al. (2014); Leitherer et al. (2016); Izotov et al. (2016, 2018, 2021); Flury et al. (2022). The high- $z$  leakers are taken from Shapley et al. (2016); Vanzella et al. (2010, 2016); Bian et al. (2017); Fletcher et al. (2019); Rivera-Thorsen et al. (2019); Marques-Chaves et al. (2021, 2022). The individual detection at  $z = 1.42$  from Saha et al. (2020) is indicated by the grey filled circle.

Thus, we have,

$$N_{LyC}^{esc} = \frac{L_{F154W} (\lambda_{mean}^{F154W})^2}{hc} e^{\tau_{IGM}} \quad (2)$$

where  $L_{F154W}$  is the luminosity computed using the observed flux in the F154W filter,  $\lambda_{mean}^{F154W} = 1541\text{\AA}$  for the F154W filter and the  $e^{\tau_{IGM}}$  term is introduced to correct for the absorption by the IGM. The IGM models used in the analysis are discussed in Section 6.1. We now use the following expression to denote the absolute escape fraction,

$$f_{esc} = \frac{N_{LyC}^{esc}}{N_{LyC}^{esc} + N_{LyC}^{non-esc}} \quad (3)$$

The estimated mean escape fractions of the 10 LyC leakers are provided in Table 1.

In Figure 3 we show the LyC  $f_{esc}$  of our sample in comparison with LyC leakers at lower and higher redshifts. It is difficult to predict any redshift evolution of  $f_{esc}$  from the distribution; however, it is important to note here that different studies use different IGM models and probe LyC at various rest frame wavelengths.

### 6.1. IGM Attenuation Models

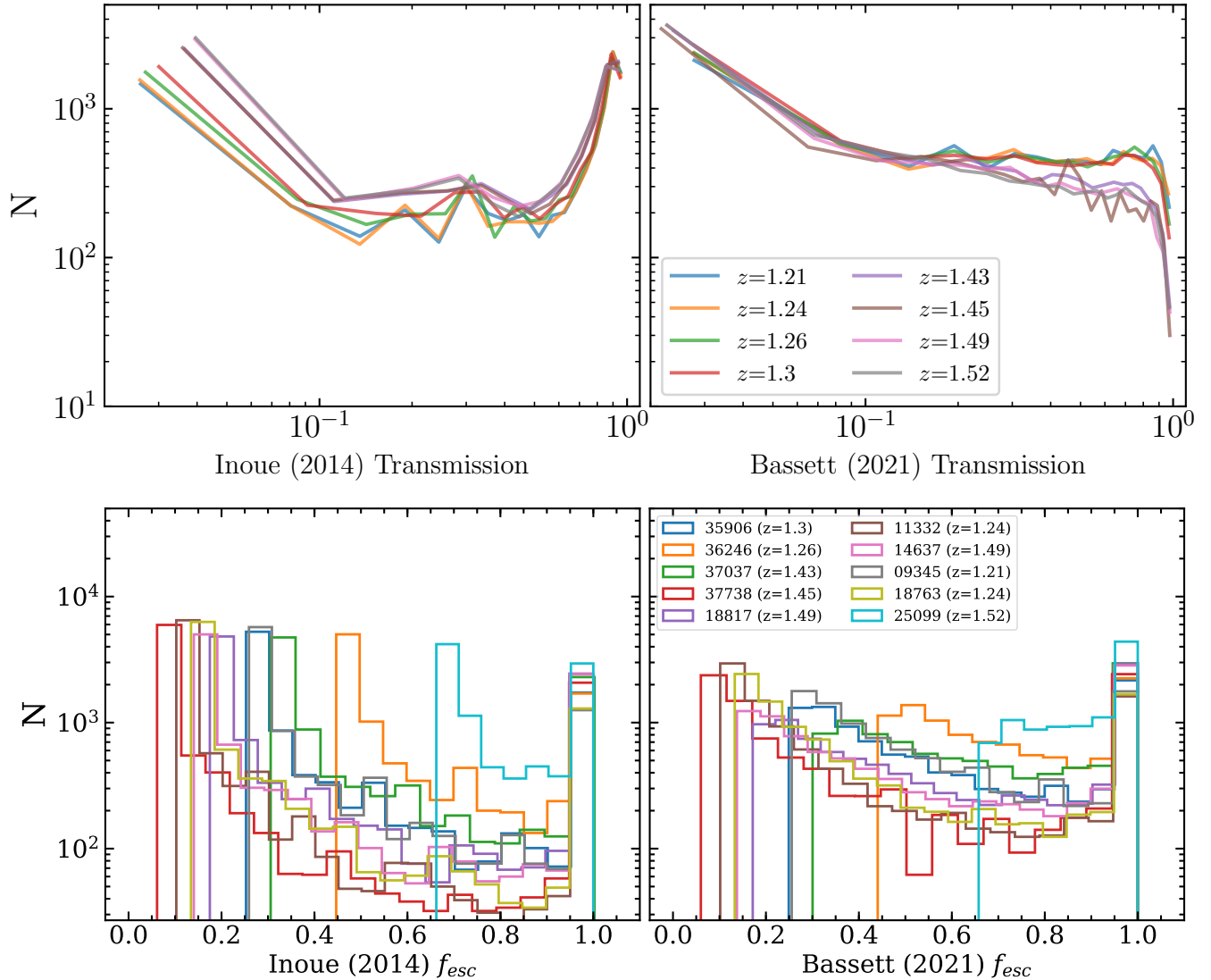


**Figure 4.** Top: The UVIT F154W-weighted IGM transmission distributions of Inoue et al. (2014) and Bassett et al. (2021) for the redshifts corresponding to the LyC leakers. Each curve was binned according to Freedman-Diaconis. The Inoue et al. (2014) simulations resulted in more clear sightlines compared to Bassett et al. (2021) for the same redshifts, which would result in lower  $f_{esc}$  (see eqn. 2 & 3). Bottom: Escape fraction distribution of the LyC leakers using IGM attenuation models from Inoue et al. (2014) on left and Bassett et al. (2021) on the right.

Since the average IGM absorption of LyC by hydrogen at a given redshift is often stronger than individual sightlines for LyC-detected galaxies, we explore the two IGM attenuation codes of Inoue et al. (2014) (hereafter I14) and Bassett et al. (2021) (hereafter B21) to model the distributions of IGM attenuation integrated through various sightlines at the redshifts of our LyC leakers. Both models use a Monte-carlo (MC) method to simulate the various sightlines, integrating the cumulative effects of damped Ly $\alpha$  absorbers (DLAs), Lyman limit systems (LLSs), and the Ly $\alpha$  forest (LAF) through the IGM at some redshift, using the spatial and density distribution statistics of these absorbers.

The most notable differences between these two codes are the absorber distribution parameters. The B21 model adopts the distributions of Steidel et al. (2018), which in turn uses HI distribution data from the Keck Baryonic Structure Survey (Steidel et al. 2004, 2010, 2014; Rudie et al. 2012; Strom et al. 2017), and also includes an optional CGM correction based on data from Rudie et al. (2013), while I14 uses LyC photon mean-free path data from Prochaska et al. (2009), O’Meara et al. (2013), Fumagalli et al. (2013), and Worseck et al. (2014). The parameters are summarized in table 1 of I14 and table 11 of Steidel et al. (2018) for the B21 model. In I14, the distributions for DLAs and LAF are computed separately and summed, while B21 use a piece-wise func-

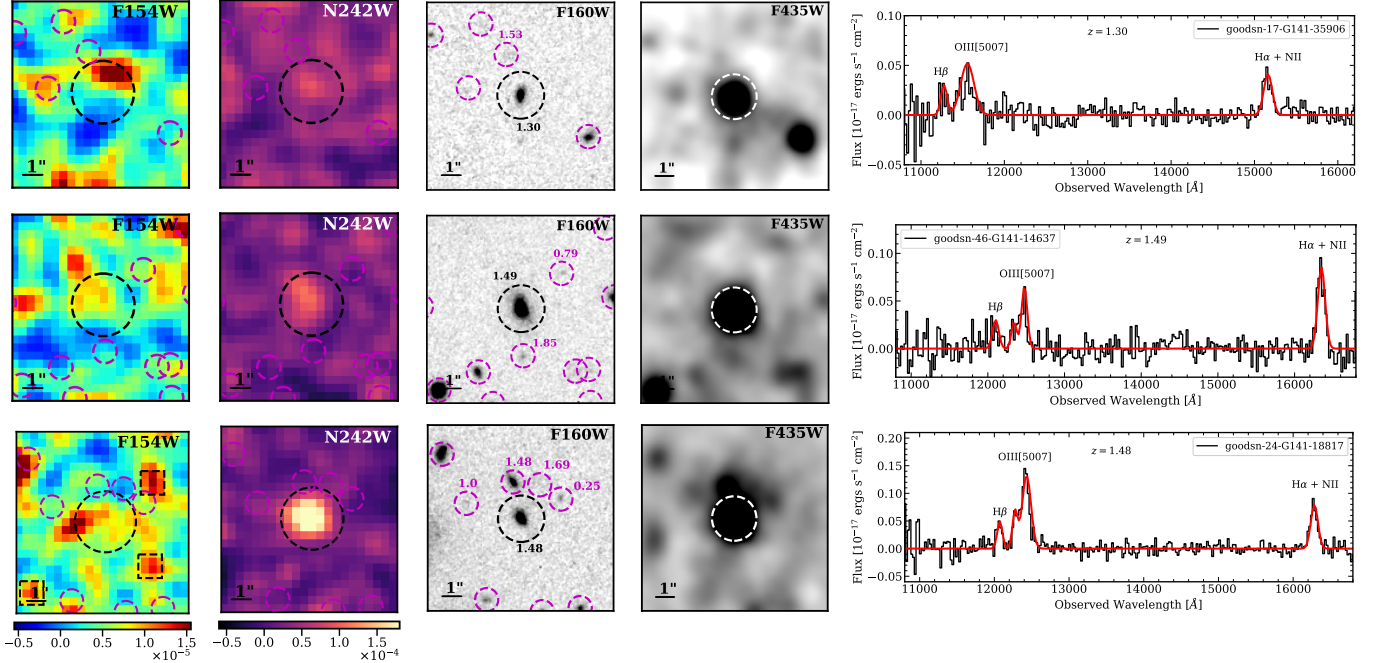


**Figure 5.** LyC leakers having off-centred or extended emission in FUV 154W band. The sequence and symbols are the same as in Figure 1. Bright peaks in the F154W image top panel at north and north-east are due to sources observed in HST F435W(not seen in the  $10'' \times 10''$ ) cutouts shown, while in the third panel the spurious sources at north-west, south-west and south-east have magnitudes (SNR): 26.61 (2.56), 26.42 (2.88) and 27.0 (2.01) respectively.

tion for the absorber distributions based on absorber density and adds the optional CGM absorption, which we do not include. These differences can lead to a higher IGM transmission in the B21 model at  $z \simeq 3-4$  vs. I14 due to the bimodal peaks in the transmission distribution of the B21 model. Furthermore, as discussed in B21, LyC detections from galaxies at  $z \simeq 3-4$  are more likely unimodal with transmission values peaking near 100%.

At the redshifts of our galaxies, we see the opposite effect, again due to the absorber distribution statistics. I14 uses an equivalent DLA redshift-distribution power law as B21 at our redshift range of interest, however I14 uses as a softer density distribution power law for DLAs ( $g(N_{HI}) \sim N_{HI}^{-0.9} \exp(N_{HI}/10^{21})$  vs  $g(N_{HI}) \sim N_{HI}^{-1.463}$  where  $g(N_{HI})$  represents the  $N_{HI}$  density distribution; see I14). This results in fewer dense absorbers ( $15 \lesssim \log(N_{HI}/\text{cm}^{-2}) \lesssim 21$ ) in the line of sight for the I14 model. We show the Astrosat UVIT F154W filter-weighted transmission for all unique redshifts and  $f_{esc}$  distributions of our LyC-leakers for both codes in Figure 4. The transmission ( $T=e^{-\tau}$ ) and  $f_{esc}$  columns in Table 1 correspond to the mean T and  $f_{esc}$  which is averaged over all lines of sights for the respective IGM models. The mean transmission for the I14 model used in this work is  $\sim 0.57$ , while the same for the B21 model is  $\sim 0.33$ . These transmission values are comparable to the transmissions of LyC at higher redshift, eg: at  $z \sim 3-4$  B21. However, the LyC transmission in B21 is

with respect to rest wavelengths of  $880 - 910 \text{ \AA}$ , whereas the LyC wavelength probed in this work is  $\sim 650 \text{ \AA}$ , a region of the LyC spectrum in which the transmission is lower.

## 7. EXTENDED LYC EMISSION

Previous works have indicated that the ionizing LyC and non-ionizing UV emissions can originate from different regions in star-forming galaxies (Iwata et al. 2009; Vanzella et al. 2010, 2012). Some of the LyC leakers in our sample show extended LyC emission beyond the UVIT PSF FWHM or off-centred emission ( $\gtrsim 1''$ ) with respect to the optical and the N242W band. The typical offset with respect to the optical centroids (estimated from HST F435W band) is  $\sim 0''.8$ , while it is  $> 1''.6$  for two cases (see Figure 5). Note that the rms of the astrometry in UVIT images is  $\sim 0''.25$  (Mondal et al. 2023).

Iwata et al. (2009) found similar offsets in the UV continuum (UVC) and LyC for a sample of Lyman Alpha Emitters (LAEs) and Lyman Break Galaxies (LBGs) at  $z \sim 3$ , with substructures in the LyC. We do not identify any substructures in the LyC because of the resolution constraints; however, the offsets and extended emission are prominently seen. For size comparison, we show the HST F435W band images (which probes the rest frame  $\sim 1500-2300 \text{ \AA}$  for the redshift range of our sample) convolved with UVIT F154W PSF in Figure 1 and 5. The ratio of LyC (F154W) to the UVC (F435W) are provided in Table 1. Our observed LyC to UVC ra-

tio is on average higher than what has been reported in the literature (Steidel et al. 2018). However, it is worth noting that previous LyC studies such as those of Steidel et al. (2018) at  $z \sim 3$  probe LyC wavelengths at  $\sim 900 \text{ \AA}$  and the UVC at  $1500 \text{ \AA}$ , whereas in this work the LyC wavelengths probed for the leakers is  $\sim 600\text{-}700 \text{ \AA}$  and the UVC corresponds to rest-frame wavelengths  $1500\text{-}2300 \text{ \AA}$ . It would be interesting to compare our observed ratio with the intrinsic ratio obtained from the best-fit intrinsic spectral energy distribution (SED) of these objects. We defer this exercise for the future.

We further produced the stack of the LyC signal of the six LyC leakers (the first six galaxies in Table 1 for which the LyC emission is within  $1''.6$ ) from the HST centroids. To construct the stack, we consider  $10'' \times 10''$  size sky subtracted F154W band images of the objects. We then mask neighbouring sources outside a  $1''.6$  aperture radius from the centroid of the source using segmentation maps produced by SExtractor with a  $1\sigma$  detection threshold. The stacked image is then produced by the average count rate of the six LyC leaking galaxies. The stacked LyC shown in Figure 6 has a total flux of  $2.75 \times 10^{-4} \text{ c/s}$  within the  $1''.6$  aperture corresponding to  $S/N \simeq 7.49$  and  $\sigma \simeq 3.0 \times 10^{-6} \text{ c/s}$ .

In previous studies by Smith et al. (2018, 2020), flat LyC profiles have been observed with average stacked LyC profiles of galaxies and weak AGNs where they associate the non-central LyC emission to the porous IGM and scattering process LyC photons undergo prior to the escape. Because of the resolution constraints we do not attempt to produce the surface brightness profile of the LyC here. Three of the galaxies show even larger offsets in LyC emission from the F160W centroids and extended emission. In Figure 5, we show these three galaxies and their spectra. Although the galaxies show very extended and off-centred emission and the source of emission could be debatable, there are no nearby sources which could be considered as possible sources of emission. Therefore, the extended emission is most probably from the host galaxies. The spatial distribution of the LyC emitting sources from that of non-ionizing UV-emitting stars can cause these offsets.

### 8. FOREGROUND INTERLOPERS AND AGN DIAGNOSTICS

As mentioned in section 2.3, the final sample of ten LyC leakers is chosen such that there are no nearby sources within a radius of  $1''.2$  in the HST images (see third panel of Figures 1 & 5). However, some fields are crowded, and surrounding objects, although not within  $1''.2$ , are close to the LyC sources. In Figure 1 & 5, the neighbouring sources are shown by dashed magenta circles on the HST F160W images. The photometric redshifts of the nearest sources are also given in magenta. The surrounding sources detected in HST detection images do not have emission in the FUV band as observed in all the middle image panels in Figure 1 & 5. Also,

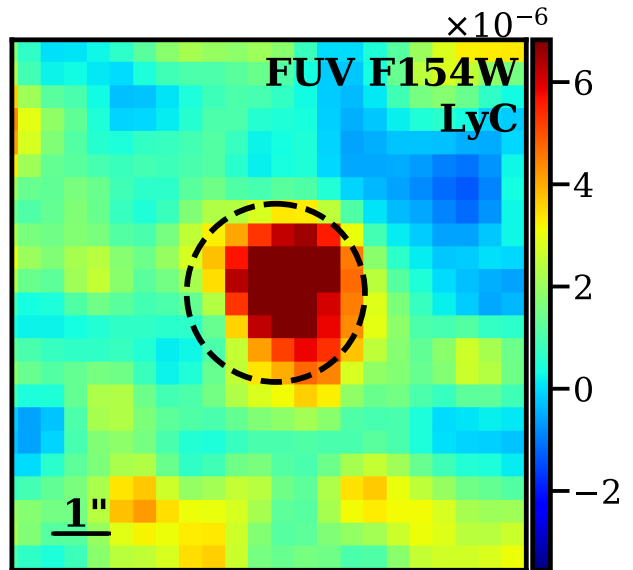


**Figure 6.** The stacked image of LyC (FUV F154W) of the six LyC leakers having emission within UVIT PSF FWHM  $\sim 1.6''$ .

the possibility of contamination from objects in the line of sight can be ruled out as the spectra do not show any other lines than the  $H\alpha$  and  $O[III]5007$  and the redshifts estimated from the grism spectra match with the photometric redshift from the Skelton et al. (2014) catalog. Hence, the estimated escape fraction is unlikely to be contaminated by the neighbouring or foreground sources.

To check if any of the objects in our sample are possible AGNs (Active Galactic Nuclei), we explored the X-ray archival data. We find that one of the sources from the sample is identified as an AGN in the 2 Ms Chandra Deep Field-North Catalog (Xue et al. 2016). The other 9 sources are classified as normal galaxies.

### 9. POSSIBILITY OF MORE LYC EMITTER CANDIDATES IN THE AUDF-NORTH

There are 20 sources in the shortlisted sample of 39 galaxies having  $2.5 < SNR < 3$  (see SNR histogram in Figure A.3). Considering the flux of the faintest source of the 20 galaxies and a mean local background, we estimate exposure time so that the sources have an  $SNR > 3$ . With an observation with effective exposure time  $> 46 \text{ ks}$  in FUV, the 20 sources would be above SNR 3. Thus, we predict the possibility of tens of more LyC detections in the AUDF Fields in the upcoming observations and the capability of UVIT.

### 10. SUMMARY

Using the deep imaging from UVIT and the grism spectra from the 3D-HST survey, we report the direct detection of LyC emission from 10 sources (9 galaxies and 1 AGN) in the GOODS-North field. The reported

LyC leakers are at the redshift of  $1.0 < z < 1.6$ , near the epoch when the cosmic star formation peaked. Using two IGM attenuation models, we provide the absolute LyC escape fraction of the detected LyC emitters. The LyC emission is seen to be off-centred and extended as compared to the optical counterpart in most of the sources in the sample. The rest frame UV wavelengths of the LyC leakers are found to be in the EUV regime (550-700Å), far below the Lyman limit (912Å) studied to date. Further, we also predict the possibility of at least tens of more LyC detections in the Astosat UVIT deep fields, which would be possible with upcoming observations.

SD and KS acknowledges support from the Indian Space Research Organisation (ISRO) funding under project PAO/REF/CP167. This publication uses the UVIT data obtained from the Indian Space Science Data Centre (ISSDC) of ISRO, where the data for AstroSat mission is archived. The UVIT project is a collaboration between IIA, IUCAA, TIFR, ISRO from India and CSA from Canada. This work is based on observations taken by the 3D-HST Treasury Program (GO 12177 and 12328) with the NASA/ESA HST, which is operated by the Association of Universities for Research in Astronomy, Inc., under NASA contract NAS5-26555.

*Facilities:* 3DHST(WFC3), ASTROSAT(UVIT)

*Software:* astropy (Astropy Collaboration et al. 2013), Source Extractor (Bertin & Arnouts 1996)

## REFERENCES

- Alavi, A., Colbert, J., Teplitz, H. I., et al. 2020, ApJ, 904, 59, doi: [10.3847/1538-4357/abbd43](https://doi.org/10.3847/1538-4357/abbd43)
- Astropy Collaboration, Robitaille, T. P., Tollerud, E. J., et al. 2013, A&A, 558, A33, doi: [10.1051/0004-6361/201322068](https://doi.org/10.1051/0004-6361/201322068)
- Bassett, R., Ryan-Weber, E. V., Cooke, J., et al. 2021, MNRAS, 502, 108, doi: [10.1093/mnras/stab070](https://doi.org/10.1093/mnras/stab070)
- Bertin, E., & Arnouts, S. 1996, A&AS, 117, 393, doi: [10.1051/aas:1996164](https://doi.org/10.1051/aas:1996164)
- Bian, F., Fan, X., McGreer, I., Cai, Z., & Jiang, L. 2017, ApJL, 837, L12, doi: [10.3847/2041-8213/aa5ff7](https://doi.org/10.3847/2041-8213/aa5ff7)
- Borghain, A., Saha, K., Elmegreen, B., et al. 2022, Nature, 607, 459, doi: [10.1038/s41586-022-04905-9](https://doi.org/10.1038/s41586-022-04905-9)
- Borthakur, S., Heckman, T. M., Leitherer, C., & Overzier, R. A. 2014, Science, 346, 216, doi: [10.1126/science.1254214](https://doi.org/10.1126/science.1254214)
- Brammer, G. B., van Dokkum, P. G., Franx, M., et al. 2012, ApJS, 200, 13, doi: [10.1088/0067-0049/200/2/13](https://doi.org/10.1088/0067-0049/200/2/13)
- Capak, P., Cowie, L. L., Hu, E. M., et al. 2004, AJ, 127, 180, doi: [10.1086/380611](https://doi.org/10.1086/380611)
- Fletcher, T. J., Tang, M., Robertson, B. E., et al. 2019, ApJ, 878, 87, doi: [10.3847/1538-4357/ab2045](https://doi.org/10.3847/1538-4357/ab2045)
- Flury, S. R., Jaskot, A. E., Ferguson, H. C., et al. 2022, ApJS, 260, 1, doi: [10.3847/1538-4365/ac5331](https://doi.org/10.3847/1538-4365/ac5331)
- Fumagalli, M., O'Meara, J. M., Prochaska, J. X., & Worseck, G. 2013, ApJ, 775, 78, doi: [10.1088/0004-637X/775/1/78](https://doi.org/10.1088/0004-637X/775/1/78)
- Gialalisco, M., Ferguson, H. C., Koekemoer, A. M., et al. 2004, ApJL, 600, L93, doi: [10.1086/379232](https://doi.org/10.1086/379232)
- Grogin, N. A., Kocevski, D. D., Faber, S. M., et al. 2011, ApJS, 197, 35, doi: [10.1088/0067-0049/197/2/35](https://doi.org/10.1088/0067-0049/197/2/35)
- Inoue, A. K., Shimizu, I., Iwata, I., & Tanaka, M. 2014, MNRAS, 442, 1805, doi: [10.1093/mnras/stu936](https://doi.org/10.1093/mnras/stu936)
- Iwata, I., Inoue, A. K., Matsuda, Y., et al. 2009, ApJ, 692, 1287, doi: [10.1088/0004-637X/692/2/1287](https://doi.org/10.1088/0004-637X/692/2/1287)
- Izotov, Y. I., Orlová, I., Schaerer, D., et al. 2016, Nature, 529, 178, doi: [10.1038/nature16456](https://doi.org/10.1038/nature16456)
- Izotov, Y. I., Schaerer, D., Worseck, G., et al. 2018, MNRAS, 474, 4514, doi: [10.1093/mnras/stx3115](https://doi.org/10.1093/mnras/stx3115)
- Izotov, Y. I., Worseck, G., Schaerer, D., et al. 2021, MNRAS, 503, 1734, doi: [10.1093/mnras/stab612](https://doi.org/10.1093/mnras/stab612)
- Kennicutt, Robert C., J. 1998, ApJ, 498, 541, doi: [10.1086/305588](https://doi.org/10.1086/305588)
- Koekemoer, A. M., Faber, S. M., Ferguson, H. C., et al. 2011, ApJS, 197, 36, doi: [10.1088/0067-0049/197/2/36](https://doi.org/10.1088/0067-0049/197/2/36)
- Koyama, Y., Shimakawa, R., Yamamura, I., Kodama, T., & Hayashi, M. 2019, PASJ, 71, 8, doi: [10.1093/pasj/psy113](https://doi.org/10.1093/pasj/psy113)
- Leitet, E., Bergvall, N., Hayes, M., Linné, S., & Zackrisson, E. 2013, A&A, 553, A106, doi: [10.1051/0004-6361/201118370](https://doi.org/10.1051/0004-6361/201118370)
- Leitherer, C., Hernandez, S., Lee, J. C., & Oey, M. S. 2016, ApJ, 823, 64, doi: [10.3847/0004-637X/823/1/64](https://doi.org/10.3847/0004-637X/823/1/64)
- Liu, Y., Jiang, L., Windhorst, R. A., Guo, Y., & Zheng, Z. 2023, arXiv e-prints, arXiv:2310.07283, doi: [10.48550/arXiv.2310.07283](https://doi.org/10.48550/arXiv.2310.07283)
- Madau, P. 1995, ApJ, 441, 18, doi: [10.1086/175332](https://doi.org/10.1086/175332)
- Marques-Chaves, R., Schaerer, D., Álvarez-Márquez, J., et al. 2021, MNRAS, 507, 524, doi: [10.1093/mnras/stab2187](https://doi.org/10.1093/mnras/stab2187)
- . 2022, MNRAS, 517, 2972, doi: [10.1093/mnras/stac2893](https://doi.org/10.1093/mnras/stac2893)
- Momcheva, I. G., Brammer, G. B., van Dokkum, P. G., et al. 2016, ApJS, 225, 27, doi: [10.3847/0067-0049/225/2/27](https://doi.org/10.3847/0067-0049/225/2/27)

- Mondal, C., Saha, K., Bhattacharya, S., et al. 2023, *ApJS*, 264, 40, doi: [10.3847/1538-4365/aca7c4](https://doi.org/10.3847/1538-4365/aca7c4)
- Nordon, R., Lutz, D., Saintonge, A., et al. 2013, *ApJ*, 762, 125, doi: [10.1088/0004-637X/762/2/125](https://doi.org/10.1088/0004-637X/762/2/125)
- O’Meara, J. M., Prochaska, J. X., Worseck, G., Chen, H.-W., & Madau, P. 2013, *ApJ*, 765, 137, doi: [10.1088/0004-637X/765/2/137](https://doi.org/10.1088/0004-637X/765/2/137)
- Osterbrock, D. E., & Bochkarev, N. G. 1989, *Soviet Ast.*, 33, 694
- Osterbrock, D. E., & Ferland, G. J. 2006, *Astrophysics of gaseous nebulae and active galactic nuclei*
- Prichard, L. J., Rafelski, M., Cooke, J., et al. 2022, *ApJ*, 924, 14, doi: [10.3847/1538-4357/ac3004](https://doi.org/10.3847/1538-4357/ac3004)
- Prochaska, J. X., Worseck, G., & O’Meara, J. M. 2009, *ApJL*, 705, L113, doi: [10.1088/0004-637X/705/2/L113](https://doi.org/10.1088/0004-637X/705/2/L113)
- Reddy, N. A., Oesch, P. A., Bouwens, R. J., et al. 2018, *ApJ*, 853, 56, doi: [10.3847/1538-4357/aaa3e7](https://doi.org/10.3847/1538-4357/aaa3e7)
- Reddy, N. A., Shapley, A. E., Kriek, M., et al. 2020, *ApJ*, 902, 123, doi: [10.3847/1538-4357/abb674](https://doi.org/10.3847/1538-4357/abb674)
- Rivera-Thorsen, T. E., Dahle, H., Chisholm, J., et al. 2019, *Science*, 366, 738, doi: [10.1126/science.aaw0978](https://doi.org/10.1126/science.aaw0978)
- Robertson, B. E., Ellis, R. S., Dunlop, J. S., McLure, R. J., & Stark, D. P. 2010, *Nature*, 468, 49, doi: [10.1038/nature09527](https://doi.org/10.1038/nature09527)
- Rudie, G. C., Steidel, C. C., Shapley, A. E., & Pettini, M. 2013, *ApJ*, 769, 146, doi: [10.1088/0004-637X/769/2/146](https://doi.org/10.1088/0004-637X/769/2/146)
- Rudie, G. C., Steidel, C. C., Trainor, R. F., et al. 2012, *ApJ*, 750, 67, doi: [10.1088/0004-637X/750/1/67](https://doi.org/10.1088/0004-637X/750/1/67)
- Saha, K., Tandon, S. N., Simmonds, C., et al. 2020, *Nature Astronomy*, 4, 1185, doi: [10.1038/s41550-020-1173-5](https://doi.org/10.1038/s41550-020-1173-5)
- Schlafly, E. F., & Finkbeiner, D. P. 2011, *ApJ*, 737, 103, doi: [10.1088/0004-637X/737/2/103](https://doi.org/10.1088/0004-637X/737/2/103)
- Shapley, A. E., Steidel, C. C., Strom, A. L., et al. 2016, *ApJL*, 826, L24, doi: [10.3847/2041-8205/826/2/L24](https://doi.org/10.3847/2041-8205/826/2/L24)
- Siana, B., Teplitz, H. I., Colbert, J., et al. 2007, *ApJ*, 668, 62, doi: [10.1086/521185](https://doi.org/10.1086/521185)
- Skelton, R. E., Whitaker, K. E., Momcheva, I. G., et al. 2014, *ApJS*, 214, 24, doi: [10.1088/0067-0049/214/2/24](https://doi.org/10.1088/0067-0049/214/2/24)
- Smith, B. M., Windhorst, R. A., Jansen, R. A., et al. 2018, *ApJ*, 853, 191, doi: [10.3847/1538-4357/aaa3dc](https://doi.org/10.3847/1538-4357/aaa3dc)
- Smith, B. M., Windhorst, R. A., Cohen, S. H., et al. 2020, *ApJ*, 897, 41, doi: [10.3847/1538-4357/ab8811](https://doi.org/10.3847/1538-4357/ab8811)
- Sobral, D., Best, P. N., Matsuda, Y., et al. 2012, *MNRAS*, 420, 1926, doi: [10.1111/j.1365-2966.2011.19977.x](https://doi.org/10.1111/j.1365-2966.2011.19977.x)
- Steidel, C. C., Bogosavljević, M., Shapley, A. E., et al. 2018, *ApJ*, 869, 123, doi: [10.3847/1538-4357/aaed28](https://doi.org/10.3847/1538-4357/aaed28)
- Steidel, C. C., Erb, D. K., Shapley, A. E., et al. 2010, *ApJ*, 717, 289, doi: [10.1088/0004-637X/717/1/289](https://doi.org/10.1088/0004-637X/717/1/289)
- Steidel, C. C., Shapley, A. E., Pettini, M., et al. 2004, *ApJ*, 604, 534, doi: [10.1086/381960](https://doi.org/10.1086/381960)
- Steidel, C. C., Rudie, G. C., Strom, A. L., et al. 2014, *ApJ*, 795, 165, doi: [10.1088/0004-637X/795/2/165](https://doi.org/10.1088/0004-637X/795/2/165)
- Strom, A. L., Steidel, C. C., Rudie, G. C., et al. 2017, *ApJ*, 836, 164, doi: [10.3847/1538-4357/836/2/164](https://doi.org/10.3847/1538-4357/836/2/164)
- Vanzella, E., Giavalisco, M., Inoue, A. K., et al. 2010, *ApJ*, 725, 1011, doi: [10.1088/0004-637X/725/1/1011](https://doi.org/10.1088/0004-637X/725/1/1011)
- Vanzella, E., Guo, Y., Giavalisco, M., et al. 2012, *ApJ*, 751, 70, doi: [10.1088/0004-637X/751/1/70](https://doi.org/10.1088/0004-637X/751/1/70)
- Vanzella, E., de Barros, S., Vasei, K., et al. 2016, *ApJ*, 825, 41, doi: [10.3847/0004-637X/825/1/41](https://doi.org/10.3847/0004-637X/825/1/41)
- Vanzella, E., Nonino, M., Cupani, G., et al. 2018, *MNRAS*, 476, L15, doi: [10.1093/mnras/sly023](https://doi.org/10.1093/mnras/sly023)
- Worseck, G., Prochaska, J. X., O’Meara, J. M., et al. 2014, *MNRAS*, 445, 1745, doi: [10.1093/mnras/stu1827](https://doi.org/10.1093/mnras/stu1827)
- Xue, Y. Q., Luo, B., Brandt, W. N., et al. 2016, *ApJS*, 224, 15, doi: [10.3847/0067-0049/224/2/15](https://doi.org/10.3847/0067-0049/224/2/15)

## APPENDIX

**Table A.1.** SExtractor Parameters Used for Detection and Photometry in F154W. Note that the DETECT.THRESH (1.2) is the relative detection threshold in terms of the background rms value above the mean local sky background.

Parameter Name	Value
DETECT_MINAREA	4
DETECT_THRESH	1.2
FILTER_NAME	default.conv
DEBLEND_NTHRESH	32
DEBLEND_MINCONT	0.01
CLEAN_PARAM	1.0
PHOT_FLUXFRAC	0.5
PHOT_APERTURES	6.71
PHOT_AUTOPARAMS	2.5, 3.5
PIXEL_SCALE	0.417
BACK_SIZE	9
BACK_FILTERSIZE	3

## A. SUPPLEMENTARY PLOTS AND TABLE

Here, we provide some of the statistics and properties of the sample. Table A.2 represents the quantities derived from the spectral analysis of the grism G141 spectra of the LyC leakers. The line fluxes mentioned in Table A.2 are corrected for foreground and internal extinction using [Schlafly & Finkbeiner \(2011\)](#) and UV  $\beta$  slope [Reddy et al. \(2018\)](#), respectively. The SFR is obtained using the corrected  $H\alpha$  line flux following [Kennicutt \(1998\)](#) that employs the Salpeter initial mass function. Whereas, to estimate the sSFR, we use the SED stellar mass from ([Momcheva et al. 2016](#)) catalogs.

Figure A.1 shows the 3D-HST grism footprint (blue polygon) over the UVIT F145W band image. The red circles represent the positions of the LyC leakers reported in the paper. Figure A.2 left panel shows the redshift distribution of the 178 shortlisted candidates having  $H\alpha$  and [OIII] line flux SNR greater than 3 (blue histogram) and the 39 sources identified in UVIT F154W band (black histogram). In the right panel of Figure A.2, we show the main sequence relation (SFR vs stellar mass) for the ten LyC leakers along with the non-leaker galaxies at the same redshift ( $1 < z < 1.5$ ). For SFR estimates of non-leakers we use the  $H\alpha$  line fluxes from [Momcheva et al. \(2016\)](#) catalogs.

Figure A.3 left panel shows the FUV 154W and N242W band magnitude distributions of the 39 sources identified in FUV 154W band of the 178 sources, while on the right is shown the F154W SNR histogram of the 39 sources.

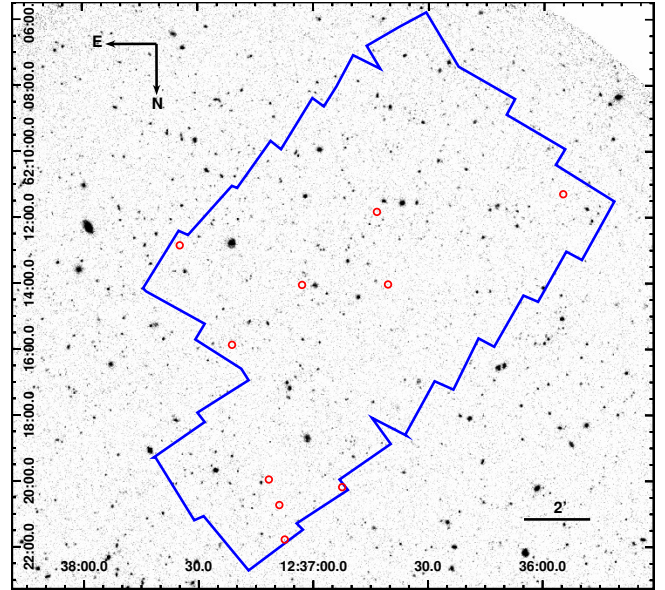


**Figure A.1.** LyC leakers indicated by red circles in the UVIT AUDF-North field. Blue polygon is the 3D-HST GOODS North spectral coverage.

**Table A.2.** Spectral Properties of the LyC emitters- Column(1): 3D-HST grism ID, Column(2): RA in hms, Column(3): Dec in dms, Column(4): spectroscopic redshift, Column(5),(6) & (7): H $\alpha$ , H $\beta$  and [OIII]5007 line fluxes, respectively in units of  $10^{-17}$  ergs s $^{-1}$  cm $^{-2}$ , corrected for foreground and internal dust extinction, column(8): SFR in units of  $M_{\odot}$  yr $^{-1}$  derived from corrected H $\alpha$  line flux and column(9): specific star formation rate (sSFR) in units of Gyr $^{-1}$ .

grism ID	RA	Dec	z	H $\alpha$ flux	H $\beta$ flux	[OIII] flux	H $\alpha$ SFR	sSFR
	hms	dms		$10^{-17}$ ergs s $^{-1}$ cm $^{-2}$			$M_{\odot}$ yr $^{-1}$	Gyr $^{-1}$
goodsn-33-G141-11332	12:36:43.42	+62:11:51.56	1.24	44.69 $\pm$ 2.46	8.93 $\pm$ 7.86	52.93 $\pm$ 6.10	31.46 $\pm$ 1.73	7.37 $\pm$ 0.41
goodsn-17-G141-36246	12:36:52.46	+62:20:12.51	1.26	6.13 $\pm$ 1.55	-	12.78 $\pm$ 3.11	4.49 $\pm$ 1.14	3.65 $\pm$ 0.92
goodsn-36-G141-25099	12:37:21.18	+62:15:53.51	1.52	2.05 $\pm$ 1.45	-	15.83 $\pm$ 4.08	2.41 $\pm$ 1.70	1.18 $\pm$ 0.83
goodsn-18-G141-37037	12:37:08.89	+62:20:45.11	1.43	10.83 $\pm$ 1.46	-	18.28 $\pm$ 2.12	10.94 $\pm$ 1.47	6.90 $\pm$ 0.93
goodsn-35-G141-18763	12:37:02.91	+62:14:04.60	1.24	31.96 $\pm$ 3.01	-	23.51 $\pm$ 5.83	22.74 $\pm$ 2.14	3.52 $\pm$ 0.33
goodsn-11-G141-09345	12:35:54.96	+62:11:18.36	1.21	12.07 $\pm$ 2.67	-	8.58 $\pm$ 4.70	8.09 $\pm$ 1.79	3.37 $\pm$ 0.75
goodsn-18-G141-37738	12:37:07.48	+62:21:47.84	1.45	119.35 $\pm$ 2.67	24.96 $\pm$ 3.11	251.82 $\pm$ 3.81	124.45 $\pm$ 2.78	1.06 $\pm$ 0.02
goodsn-17-G141-35906	12:37:11.62	+62:19:58.62	1.30	15.52 $\pm$ 2.07	13.29 $\pm$ 4.41	41.06 $\pm$ 5.79	12.41 $\pm$ 1.66	6.51 $\pm$ 0.87
goodsn-46-G141-14637	12:37:34.75	+62:12:52.38	1.49	27.28 $\pm$ 2.47	14.29 $\pm$ 4.94	32.66 $\pm$ 4.62	30.34 $\pm$ 2.74	4.09 $\pm$ 0.37
goodsn-24-G141-18817	12:36:40.52	+62:14:03.57	1.49	23.44 $\pm$ 1.96	15.61 $\pm$ 3.04	78.74 $\pm$ 3.91	25.85 $\pm$ 2.16	19.16 $\pm$ 1.60

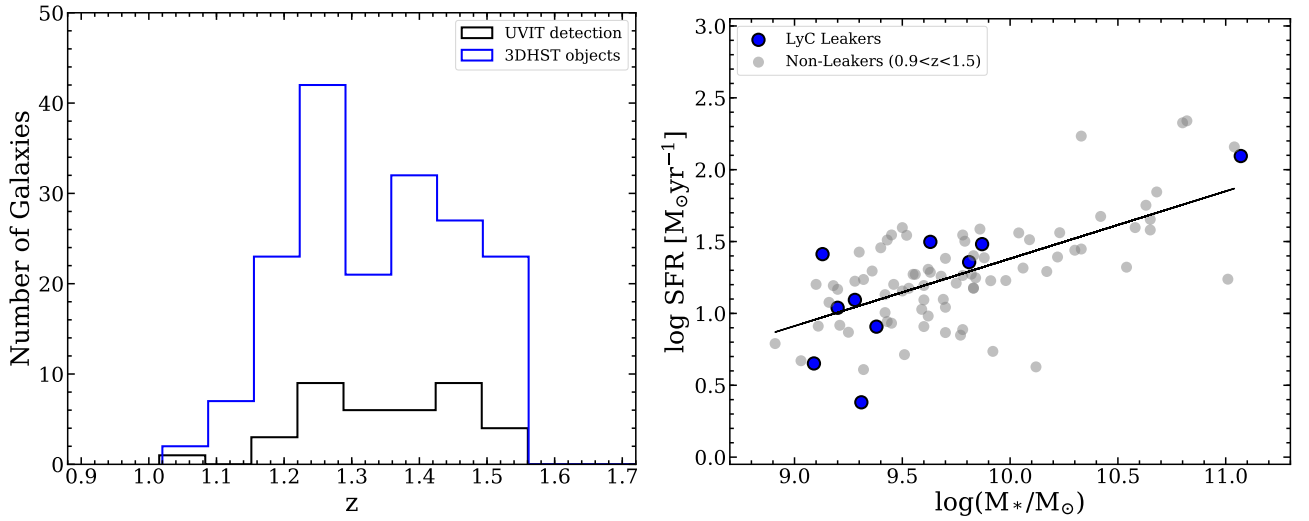


**Figure A.2.** Left- Redshift histogram of sources having H $\alpha$  and O[III] flux SNR  $>$  3 and redshift  $<$  2 (Blue) and those having detection in UVIT FUV (39 sources) out of 178 sources selected from 3D-HST. Right- SFR-stellar mass plot of the LyC leakers (blue filled circles) along with other non-leaker galaxies (gray filled circles) at  $1 < z < 1.5$ . The solid black line is a linear fit to the sample with a slope of 0.46.

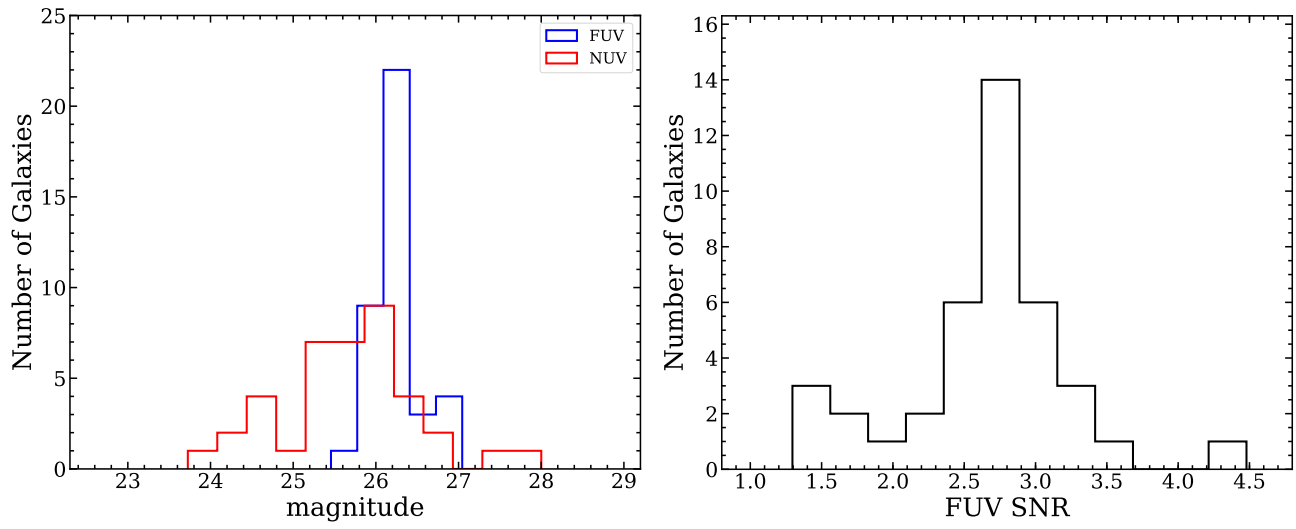


**Figure A.3.** Left-FUV magnitude distribution of clean sources having detection in UVIT FUV (39 sources) out of 178 sources selected from 3D-HST. Right-FUV SNR distribution of 39 clean sources.